Forensic Science International: Reports 13 (2026) 100443

Contents lists available at ScienceDirect

Forensic Science International: Reports

journal homepage: www.sciencedirect.com/journal/forensic-science-international-reports

General forensics

Forensic reconstruction of an incident scene using rigid body photogrammetry techniques

Kevin Gilmore [a,b], Geoffrey T. Desmoulin [a,*], Szymon Claridad [a], Marc-André Nolette [a], Theodore E. Milner [a,c]

[a] GTD Scientific, Inc., Vancouver, Canada
[b] School of Biomedical Engineering, University of British Columbia, Vancouver, Canada
[c] Department of Kinesiology and Physical Education, McGill University, Montreal, Canada

ARTICLE INFO

Keywords:
Photogrammetry
Reverse projection
Digital forensics
Scene reconstruction
Ray pinning

ABSTRACT

Forensic biomechanics is used to draw conclusions about incident and injury reports, relying on images of the incident for relevant photogrammetric measurement techniques, such as spatial resection and intersection. However, these techniques rely on the quality and type of media available, which can vary substantially. As such, this study aims to quantify the error associated with utilizing various supporting media. A simulated incident scene containing 2 objects of interest, a model rifle and a motorcycle, was 3D scanned and recorded from 3 camera angles. PhotoModeler was used to measure the 3D location of these objects with supporting media being limited to the use of a 3D scan, calibrated or uncalibrated cameras, single or multiple viewing angles, and stationary or moving cameras. The results of statistical analysis demonstrated that, when supported by a scan, single and multiple camera angles resulted in similar positional measurement errors. Mean errors of 6.52 cm and 5.98 cm for the single view, compared to ranges of 3.73–5.71 cm and 2.56 – 13.74 cm with multiple views, were found for the motorcycle and rifle, respectively. Also, using 3 stationary cameras resulted in lower distance and orientation errors than 3 frames from a moving camera. Thus, it was concluded that supporting 3D scans provide the highest level of accuracy and the use of single or multiple stationary cameras demonstrated higher accuracy compared to mobile cameras. Using 3D scans in conjunction with stationary cameras provides reliability and admissibility of photogrammetry-based evidence in forensic investigations.

Introduction

In forensic investigations, it is often required to digitize, analyze, or measure objects in a scene based on on-site video recordings, such as those from security cameras, photographs taken after the fact, or other forms of digital media, including 3D scans of the site. The data collected from these media are often used in conjunction with information such as medical reports, witness statements, and other case-specific information to draw or support conclusions instrumental to the event being investigated. As such, ensuring that accurate measurements can be made is essential to validating the techniques used in such an analysis.

The techniques used to analyze an incident scene from 2D video and photographs are generally referred to as photogrammetry. Two common techniques employed in photogrammetry are spatial resection and spatial intersection. Spatial resection uses known 3D points, such as from a 3D scan or other form of site survey, to establish the camera's orientation by correlating the known points to shared features on the camera's 2D image through a strict mathematical relationship [1–5]. Therefore, it can be effectively used in single image scenarios. An alternative to spatial resection is bundle adjustment, which uses the correlation between points across multiple images in an iterative algorithm to simultaneously determine camera and distortion parameters [6, 7]. Bundle adjustment can be performed without explicit 3D information to solve for camera locations when using multiple images, though this only gives the relative positioning of cameras. By identifying the same point across multiple camera views, spatial intersection can triangulate the point's 3D position by using the stereographic relationship between cameras t [7–9]. Furthermore, by solving for the positions of multiple points, the 3D location and dimensions of objects of interest, distances between points, height of subjects, etc, can be calculated. Measurements of the position and orientation of objects at different times can also be used to calculate velocity and acceleration, or movement paths of the

* Corresponding author.
E-mail address: gtdesmoulin@gtdscientific.com (G.T. Desmoulin).

https://doi.org/10.1016/j.fsir.2025.100443
Received 14 July 2025; Received in revised form 10 December 2025; Accepted 12 December 2025
Available online 15 December 2025

objects by utilizing timing information embedded in video files [1]. Accurate measurements also require correction for lens distortion of the image caused by non-uniformity of the lens, misalignment of optical components, and misalignment of the camera's sensor to the projected image plane [10].

Spatial resection, intersection, and other photogrammetry techniques have a wide range of application in forensics, but are also applicable in other fields of study, including motor vehicle accident reconstruction [12–20], human subject identification [11,21], biomechanics and medicine [22–28], and sports analysis [29–35]. In motor vehicle accident reconstruction, photogrammetry is used to determine vehicle speed and acceleration [19,20], analyze crash kinematics [13–15,18], and to document the crash site [12,16,19]. When attempting to identify a person of interest in an investigation, these techniques are often used to determine subject height and other identifying characteristics from 2D security camera video [11]. In the medical and biomechanical fields, photogrammetry is often used for postural or gait analysis [22–24], biomechanical analysis of humans performing specific tasks, often involving complex movements [26,28], and as a diagnostic tool [25,27]. In the sports industry, these techniques may be used to investigate the kinematics of impacts, especially in relation to head injuries [30,33,35], or to analyze the performance of an athlete or sports equipment [29,31].

Given the importance of photogrammetry in forensic investigations, it is important to determine the accuracy of photogrammetry techniques as they relate specifically to real-world conditions. The present study was designed to determine the accuracy of photogrammetry when applied to a simulated forensic investigation scene under various conditions.

Methods

The overall methodology for assessing the accuracy of spatial intersection (ray pinning) is illustrated in Fig. 1.

Simulated incident scene

This simulated forensic investigation scene, located in the rear alleyway of a suburban house, contained evidence markers and two objects of interest, namely a replica rifle and a motorcycle (Fig. 2). The model rifle was placed on the ground on its side, and the motorcycle was set on its kickstand, with its side facing generally towards camera 2. There was no direct interaction with either object after placement to prevent movement over time. Three stationary cameras and reference markers, physical 2D geometric pattern fiducial markers, were positioned at the scene for the purpose of obtaining a calibrated 3D scan of the scene. These fiducial markers create unique tracked reference points to align and register different geographic volumes of the 3D scan over larger areas, meant to improve the scan accuracy and reduce drift over distance. They were spread evenly throughout the scene, with priority given to surfaces which are otherwise difficult to scan, such as uniform pavement, or areas otherwise lacking recognizable features. This setup is intended to simulate an incident scene which a forensic specialist may be required to investigate. The cameras were placed at different heights and locations to view the scene and objects of interest from various angles, such that there was overlap between the fields of view of the different cameras to ensure that all views contained the objects of interest and a minimum of overlapping recognizable physical features of the surrounding site. While this is meant to replicate the various camera angles and positions found in real-world investigations, both from on-site cameras and investigator photos, it must be acknowledged that actual sites may have cameras placed at differing distances from the scene, at various heights, with differing resolutions and frame capture rates, and with a more obstructed view compared to the experimental setup.

The cameras, labeled as Camera 1, Camera 2, and Camera 3, were placed at heights of 1.3 m, 1.7 m, and 1.4 m above ground level, respectively, and placed on tripods to prevent movement while imaging. The 3 cameras were placed approximately in line with one another, with Camera 1 on the right and Camera 3 on the left. The distance between Cameras 1 and 2 was 3.3 m, and 6.3 m between Cameras 2 and 3. All cameras were oriented to face the center of the scene, ensuring that all objects of interest were within view, though the motorcycle was partially obstructed in the view of Camera 1 by a vertical column. The objects of interest were placed at the distances listed in Table 1 and shown in Fig. 2. These distances were first manually measured for approximation and then confirmed in the 3D scan, which included all scene features, the objects of the interest, and the camera stations.

Fig. 1. Illustration of the steps involved in calculating the error between the true position of an object and its calculated position based on photogrammetry using the method of ray pinning.

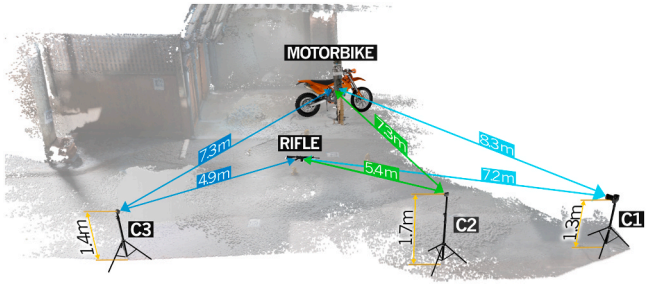

Fig. 2. Scene schematic depicting approximate placement of objects and cameras.

Table 1
Distances between object and camera, measured along the ground plane through a top-down view.

Camera	Distance to Object Geometric Center (m)	
	Motorcycle	Rifle
1	8.3	7.2
2	7.3	5.4
3	7.3	4.9

3D Scanning and processing

To document the scene, the area was 3D scanned using a Dot3D DPI-10-SG structured light scanner with an Intel RealSense D415 stereoscopic depth sensor attachment. In this way, the location and orientation of all objects and background features were recorded digitally. Care was taken to follow the loop-closure methodology for the scan, where already scanned areas are returned to frequently to aid with registration of different sections of the scene, as recommended for the Dot3D software [36]. A maximum scan range of 1.5 m to the surface being scanned was also implemented. Though the D415 manufacturer specifies an ideal operational range of up to 3 m [37], a 1.5 m maximum range was used as it has been shown that the D415 has a depth error of approximately 0.509 ± 3.9 mm within a scanning range of 0.5 – 1.5 m [38]. Scan frames were registered to one another using Dot3D's embedded software with the aid of the physical fiducial markers to minimize errors arising from drift. The scan, as well as all imagery, was completed at approximately noon on a semi-overcast day, with imaging immediately following scanning to limit changes to the scene and objects of interest. To further process the scan, CloudCompare V.2.13.1 was used to clean artifacts, remove unnecessary data points, and subsample the scan for computational efficiency. A copy of the scan with the objects of interest removed, through a combination of manual removal of points and filtering, was also generated to be used as a reference scan for photogrammetry, providing the basis for performing the required measurements and replacing missing objects of interest. The removed objects were saved as individual point clouds to be used as representative 3D models of the objects of interest to be replaced into the scene.

The ability to accurately place objects in a forensic incident scene is dependent on the type of incident data and camera information available and how the data are processed. There may be images from one or more cameras, the cameras may be stationary or moving, and it may or may not be possible to pre-calibrate the cameras to correct for lens distortion through known-pattern calibrations or other techniques. Therefore, all of these possibilities were considered in the analysis with the cameras detailed in Table 2.

Calibration for lens distortion correction was completed prior to the experiment, using a multi-sheet grid set up with known geometry to define camera lens characteristics. A 3 × 3 multi-sheet grid was placed on the ground and the cameras recorded images of all 4 sides of the grid (Fig. 3). In addition, each camera was rotated 90 deg clockwise and 90 deg counterclockwise and the same images were again recorded, resulting in 12 total calibration images. After being uploaded to PhotoModeler Premium software, version 2025.0.0.332 (PhotoModeler Technologies, Vancouver, British Columbia, Canada), the lens distortion of each camera, necessary to correct the grid's geometry, was determined using PhotoModeler's built-in calibration function. No built-in correction functions, such as the Linear view on the GoPros, were used.

Table 2
Specifications of the cameras used in testing.

	Model	Resolution (pixels)	FPS
Camera 1	Canon EOS 7D	1280	60
Camera 2	GoPro Hero 8	2.7 K	60
Camera 3	GoPro Hero 11	5.3 K	60
Camera 4	Axon Body 2	848 × 480	30
Camera 5	Samsung Galaxy S22 Mobile Phone	2160 × 3840	60

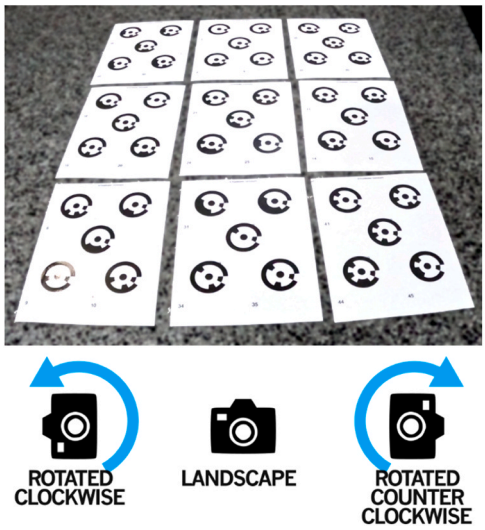

Fig. 3. The multi-sheet grid used for camera calibration. Twelve images were recorded from approximately 45 deg to the horizontal, one from each side, and this was repeated with the camera rotated 90 deg clockwise and counterclockwise.

The resulting distortion parameters can be found in Table 3, in the format used by PhotoModeler. PhotoModeler uses the following equations to correct for radial and decentering lens distortion respectively [39].

$$dr = K1 * r^2 + K2 * r^4 + K3 * r^6 \quad (1)$$

$$dpx = P1 * \left(r^2 + 2 * x^2\right) + 2 * P2 * X * Y \quad (2a)$$

$$dpy = P2 * \left(r^2 + 2 * y^2\right) + 2 * P1 * X * Y \quad (2b)$$

In Eq. (1), r is the radial distance from the principal point and $K1$-$K3$ are radial distortion coefficients solved through the calibration process. In equation (2), X and Y are image coordinate components, and $P1$ and $P2$ are dicentric distortion coefficients solved in the calibration process. The calibration also solves for format size, principal point, and focal length [39]. Note that PhotoModeler solves for focal length as a principal distance. PhotoModeler also often provides scaled values for focal length, principal point, and format size, resulting in values that do not match those given for the camera or respective lens, or those in Table 2. The resulting RMS residual plots for each camera's calibration are presented in Appendix A. Self-calibration, using bundle adjustment for multi-photo projects and a hybrid algorithm for single photo projects [39], on the simulated scene images was also completed for each camera in each condition given below, including the uncalibrated camera conditions, in which this pre-calibration through the known-pattern grid was not applied.

A study by Kraszewski in 2011, analyzed how different calibration techniques affected the interior parameters of a camera [40]. Alhough using a single sheet calibration rather than the multi-sheet used in the present study, they demonstrated that this calibration method produced accuracy results of within 0.7 μm and 1.2 μm for focal length and principal point respectively, based on their specific calibrations [40]. When confirming calibration results by measuring known control points on a 3D test rig, the PhotoModeler sheet calibration method showed control point measurement RMSE values of between 0.28 and 0.83 mm depending on camera focal length (24, 35, and 50 mm) [40]. This calibration method has also been used in other published literature and shown to produce good final measurement results in various

Table 3
Calibration parameters solved through PhotoModeler's known-pattern calibration methodology. No significant correlation between parameters was reported by PhotoModeler.

	Camera Model	K1	K2	K3	P1	P2	Focal Length	Format Size		Principal Point	
								W	H	X	Y
1	Canon EOS 7D	3.373e-03	-4.459e-05	0	-1.241e-04	8.556e-05	7.8173	9.0194	5.0625	4.5929	2.4292
2	GoPro Hero 8	7.520e-03	3.282e-05	0	-8.370e-05	-2.576e-05	6.3451	9.0972	5.0592	4.5760	2.5719
3	GoPro Hero 11	7.089e-03	6.304e-05	0	2.857e-05	0	6.2927	9.0021	5.0625	4.5015	2.5277
4	Axon Body 2	1.857e-02	1.217e-04	3.307e-05	4.149e-04	4.116e-04	4.8704	9.0143	5.0943	4.4489	2.4075
5	Samsung Galaxy S22	-5.491e-04	0	0	0	0	7.6025	5.0561	9.0000	2.5022	4.4772

applications [41–43].

Experimental conditions

Table 4 lists the conditions which were compared for position and orientation spatial intersection errors.

Condition 1 used single cameras with a 3D scan, a necessity for single camera projects as the scan provides the 3D scene coordinates required for locating the camera and performing self-calibration. Self-calibration was completed using at least 25 matching control points, as recommended by PhotoModeler, seen in both the 2D image and 3D scan (Fig. 4). The location and orientation of the cameras is solved to minimize the error between known control points from the site 3D scan when seen through the view of the camera, while simultaneously solving for lens distortion by determining how the 2D image must be corrected to further minimize the error between control points and related points marked on the image. Therefore, perfect alignment would result in features seen in the 2D image, aligned with the same features in the 3D scan when viewed from the solved camera location. For this condition, individual measurements were made for each camera, using Cameras 1–3 as documented in Table 1.

Conditions 2–4 used images recorded simultaneously with Cameras 1–3 from three viewpoints. These conditions differed according to whether the scan was used as in condition 1, whether the pre-calibration was used instead, or whether the images were uncorrected for lens distortion (uncalibrated). The 3D scan was not necessary for the 3-camera solution as the three viewpoints were used to triangulate points of interest. By triangulating these points, the relative position and orientation of each camera to the others could be solved. If the cameras have not been calibrated, this step also attempts to solve for image distortion through bundle adjustment self-calibration, so it is recommended by Photomodeler to place at least 25 shared points. In these cases when a 3D scan was not used as a reference, the project lacks a defined scale. Therefore, physical measurements were taken at the scene and used within Photomodeler to generate a scene-wide scale. These scaling measurements were defined for the 3 coordinate axes.

Conditions 5–7 were similar to conditions 2–4 as to whether the 3D scan or pre-calibration was used. However, instead of three separate stationary cameras, a single, moving camera was used to record video.

Table 4
Testing conditions used for analysis.

Condition	Cameras	3D Scan	Cameras Pre-Calibrated	Number of Data Sets
1 Single Stationary	C1, C2, C3)	Yes	No	3
2 Combined Stationary	C1, C2, C3	Yes	No	1
3 Combined Stationary	C1, C2, C3	No	Yes	1
4 Combined Stationary	C1, C2, C3	No	No	1
5 Moving	C4, C5	Yes	No	2
6 Moving	C4, C5	No	Yes	2
7 Moving	C4, C5	No	No	2

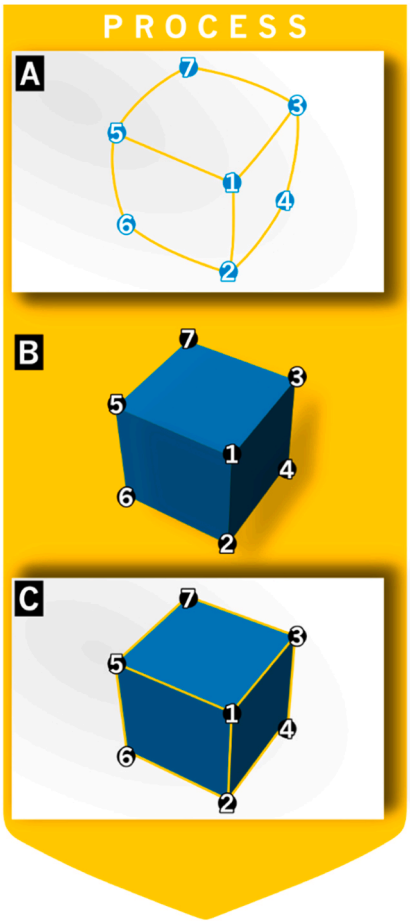

Fig. 4. The process of performing self-calibration using a 3D scan in PhotoModeler. (A) The 2D image has points selected at prominent features. (B) The same points are selected in the 3D scene scan. These points have known 3D coordinates (C) The two sets of control points are correlated and matched to solve for lens distortion parameters and undistort the image through a hybrid bundle adjustment algorithm [39].

Video frames from different points in time, and therefore distinct positions, were extracted and the same method was used as with the 3-camera solution to solve for the camera's position at each frame. Conditions 5–7 were performed for Cameras 4 and 5 separately. The moving camera (Axon Body 2, Samsung Galaxy S22) was strapped to a person moving through the scene at an approximate jogging speed. Video was recorded during this movement. For the purpose of analysis and measurement, the cameras were moved along a path in which all objects of interest were visible at some point during the recording.

Ray pinning (spatial intersection)

The 2D videos recorded by each camera were uploaded to

PhotoModeler and corrected for lens distortion through camera calibration for conditions in which cameras were pre-calibrated as specified in Table 4. The camera locations were solved using the methods described above dependent on whether or not a 3D scan was employed. Ray pinning, PhotoModeler's terminology for the process of using spatial intersection techniques to place 3D objects in a scene, was then performed. For multiple images, ray-pinning within PhotoModeler uses the principles of spatial intersection to define the 3D location of specific features or distinct marks seen on the object of interest, in this case the motorcycle or rifle. Once these are defined, the same features or marks are selected on a digital 3D model of the object, which in this case is a 3D scan of the objects of interest. The 3D model of the object is positioned relative to the cameras based on the best-fit between the position of the points solved through spatial intersection and their position on the 3D model of the object. An accurate solution would place the digital 3D object in the same relative position to the virtual camera as the relative position of the physical object of interest to the physical camera when the image was taken. A minimum of 3 points is required for this process. For single cameras, spatial intersection cannot be used to solve for the 3D coordinates of the points on the 2D image. Instead, lines are projected from the previously solved camera source through the selected 2D points on the object of interest in the image. The corresponding selected points on the 3D model are then aligned with the ray projection lines originating from the camera. However, this will only constrain the placement of the 3D object model in the focal plane of the camera. The known size of the object constrains its distance from the camera, as the conical shape of the projected lines will best-fit the points on the 3D model of the object at a specific distance from the camera. Fig. 5 illustrates the selection of the common points on the 2D image and the 3D model of the object of interest. With a sufficient number of points, all 6 ° of freedom, defining the position and orientation of the model can be solved by optimization. As our 3D model was a direct scan of the specific objects of interest, scale was not included as a solvable degree of freedom. However, when investigators must use 3D object models which are not exactly the same as the specific object of interest, scale will need to be considered as well.

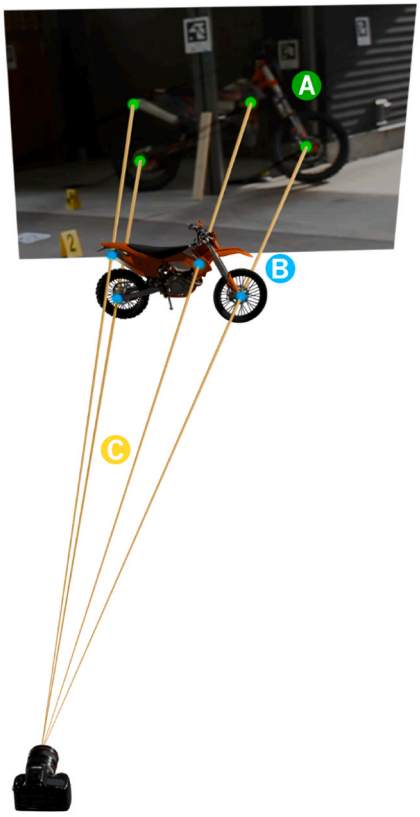

Fig. 5. The process of ray pinning a model using a single camera, oriented through use of a 3D site scan. A. The 2D image with marked points on distinct features of the motorcycle. B. The digital 3D object representation with points marked on the same features as in A. C. The object model is orientated according to the best match between the rays formed between the camera origin and the marked points on the 3D model. The marked points of the object model are placed along their respective rays in 3D space and, based on the known dimension of the object, a constrained solution is obtained.

After ray pinning the object models, they were exported from PhotoModeler into CloudCompare. However, in order to maintain the same coordinate system as the known position and orientation of the objects of interest, the placed object model had to be exported with the site scan point cloud as well. Therefore, the exported point cloud was manually processed and filtered to retain only the ray-pinned model of the object of interest. The integrity of this model, relative to the known reference model, was confirmed by comparing characteristics such as point count, volume, and bounding box dimensions. If all characteristics matched, the exported pinned model was deemed to be acceptable, allowing error calculation to be performed.

Error calculation

For the purpose of generalization to any camera system, the positions of the 3D points representing the reference scan of the object and the 3D points representing the ray-pinned, overlaid model, were transformed to the coordinate system of each camera. The camera position and orientation parameters provided by PhotoModeler were used to translate and rotate the data points such that the origin of the coordinate system was shifted to the center of the camera, with the x-axis representing left-to-right in the camera's focal plane, the y-axis representing bottom-to-top in the camera focal plane and the z-axis representing the optical axis of the camera, using a right-handed convention. Position error between the actual object and the overlaid model was determined by calculating the mean difference between corresponding points in the point cloud of the reference scan of the object and the point cloud of the ray-pinned, overlaid model. The error was expressed as absolute error in the xy plane (r_{xy}) and along the z-axis (r_z), as well as the total error (r_{xyz}). To find the orientation error around each coordinate axis, the positions for corresponding 3D points on the reference scan of the object and the ray-pinned, overlaid model were projected onto each coordinate plane as shown in Fig. 6A. The red circles in Fig. 6A represents the 2D projections of a 3D point on the scanned object onto the xy, xz and yz planes and the green circles represent the corresponding projections of the 3D ray-pinned object. The colored arrows in Fig. 6B represent the 2D vectors from the origin of the coordinate system. The black arrows, perpendicular to each plane, represent the cross product vector of the two colored vectors in the corresponding plane, i.e. $u \times v$ in Eq. (3) below. The signed angle between each pair of vectors in a plane was calculated from the cross product on the vectors and the inverse sine function, i,e. Eq. (4), providing the signed difference in orientation around the axis perpendicular to the plane as shown in Fig. 6C.

$$u \times v = |u||v|\sin\theta \tag{3}$$

$$\theta = \sin^{-1}\frac{u \times v}{|u||v|} \tag{4}$$

For example, in the case of the z-axis (xy plane), vector u would be (x_r,y_r) and vector v would be (x_s,y_s) where the subscript r refers to the position of the overlaid, ray-pinned model and the subscript s refers to the position of the reference scan of the object. The absolute value of the mean difference in orientation over all 3D points in the object representation was taken as the orientation error.

In the case of single camera views (condition 1), there was only a single error value for each variable. However, for conditions 2–4, where the views from three cameras were combined, it was possible to

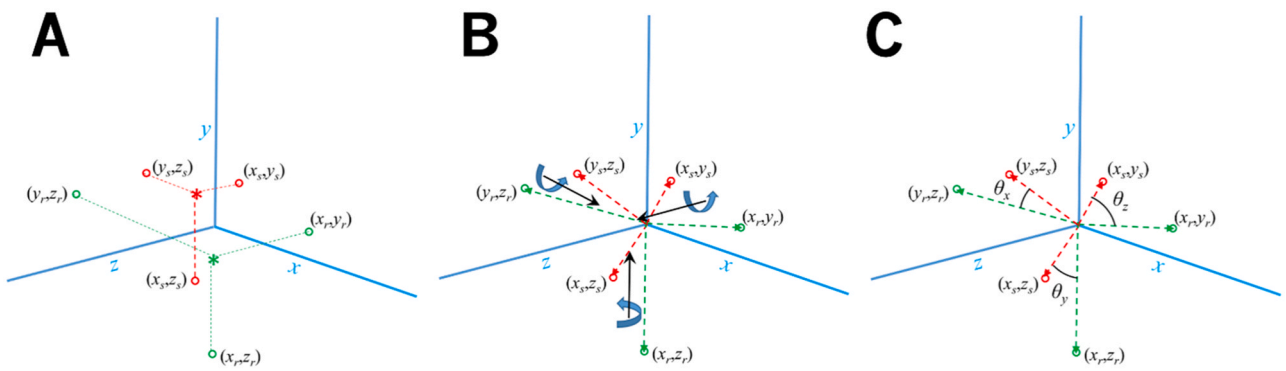

Fig. 6. A. Corresponding points on the surface of the reference scan of the object (subscript *s*) and the ray-pinned object (subscript *r*) are illustrated by green and red asterisks, respectively. Their 2D projections onto the *xy*, *xz* and *yz* planes are represented by the corresponding colored circles. B. The 2D vectors to the corresponding projected points are shown as dashed green and red arrows. Black arrows represent the cross-product vectors of the green and red vectors, showing the direction of rotation for calculating the orientation error angles. C. Orientation error angles determined from the cross-products are shown for each coordinate axis.

calculate an error value for each variable from the viewpoint of each of the three cameras. To obtain a single error value for each variable, for the purpose of statistical analysis, the average of the error from the viewpoint of each of the three camera was used. Similarly, for conditions 5–7, where an error was calculated for each of the three camera positions, the average of the error from the viewpoint of each of the three positions was used. This was done for each of the five video frames in the data set.

Statistical analysis

ANOVA was performed to test the following hypotheses.

i. Ray pinning from images taken with a single camera results in greater model overlay errors along the optical axis of the camera than in the focal plane of the camera.
ii. Ray pinning from the combined images taken with three stationary cameras results in lower model overlay error than ray pinning from the individual images taken with the same stationary cameras.
iii. Using the 3D scan or calibrated cameras for ray pinning results in lower model overlay error than using uncalibrated cameras.
iv. Ray pinning from images taken by three stationary cameras results in lower model overlay error than ray pinning with from images taken at three different locations with a moving camera.

Results

The statistical results below have been organized according to the hypothesis being tested.

i. First Hypothesis

The mean errors and standard deviations for the three single camera model placements of condition 1 (N = 15) are listed in Table 5. Comparing r_z and r_{xy} errors we found

- r_z error significantly less than r_{xy} error for motorbike ($p = 0.0106$)
- r_z error significantly less than r_{xy} error for rifle ($p = 0.004$)

This result confirms the first hypothesis.

i. Second Hypothesis

Comparing errors for stationary single camera images to combined 3 camera images, we found

- r_{xyz} error not significantly different for motorbike ($p = 0.19$) or rifle ($p = 0.051$)
- for motorbike θ_z error ($p = 0.005$), θ_y error ($p < 0.0001$) and θ_x error ($p = 0.017$) significantly lower for combined than single camera images
- for rifle θ_z error ($p < 0.0001$) and θ_y error ($p < 0.0001$) significantly lower for combined than single camera images, θ_x error ($p = 0.39$) not significantly different

. Although, the results of the ANOVA indicate that the second hypothesis was not confirmed, the failure to find support for the second hypothesis can likely be attributed to the large standard deviation (high variability) in the distance error of the single camera views (condition 1).

i. Third Hypothesis

To simplify reporting of the results for conditions 2–7, only the model overlay error ranges for the means of the five video frames are listed in Table 6.

Comparing distance errors for the three calibration methodologies, we found

- for motorbike r_{xyz} error significantly lower for scan and calibrated conditions than for uncalibrated condition ($p < 0.0001$)
- for rifle r_{xyz} error significantly lower for scan condition than for calibrated condition and for both scan and calibrated conditions r_{xyz} error lower than for uncalibrated condition ($p < 0.0001$)

Table 5
Mean position and orientation errors with standard deviations for conditions 1 and 2 (N=15).

Condition		r_{xyz} (cm)	r_{xy} (cm)	r_z (cm)	θ_z (deg)	θ_y (deg)	θ_x (deg)
1	Motorbike	6.52 [4.51]	2.41 [0.75]	5.81 [4.74]	0.45 [0.32]	0.08 [0.04]	0.08 [0.04]
1	Rifle	5.98 [3.59]	2.39 [1.43]	5.39 [3.41]	0.16 [0.12]	0.04 [0.03]	0.05 [0.04]
2	Motorbike	3.73 [0.06]	3.06 [0.06]	1.81 [0.04]	0.92 [0.01]	0.19 [0.01]	0.13 [0.02]
2	Rifle	2.56 [0.42]	1.93 [0.22]	1.48 [0.44]	0.53 [0.08]	0.17 [0.03]	0.03 [0.01]

Table 6
Position and orientation error ranges for 3-camera views (N = 15).

Object	Method	r_{xyz} (cm)	θ_z (deg)	θ_y (deg)	θ_x (deg)
Motorbike	Scan	3.73–5.71	0.21–1.08	0.06–0.36	0.05–0.13
Motorbike	Calibrated	7.47–65.44	0.97–9.31	0.20–3.00	0.05–0.71
Motorbike	Uncalibrated	14.72–138.78	1.22–27.12	0.10–5.90	0.10–2.53
Rifle	Scan	2.56–13.74	0.03–0.53	0.03–0.17	0.03–0.12
Rifle	Calibrated	1.55–92.97	0.12–1.49	0.05–1.26	0.12–1.97
Rifle	Uncalibrated	23.58–125.81	2.00–6.41	0.89–11.89	0.44–8.21

It should be noted, that in the absence of a scan, distance and orientation errors were sometimes large, particularly when cameras were uncalibrated, highlighting the importance of using 3D scans to document incident scenes. The results are illustrated in Fig. 7.

Comparing orientation errors for the three calibration methodologies, we found

- for motorbike θ_z error ($p = 0.0068$), θ_y error ($p = 0.0135$) and θ_x error ($p = 0.0004$) were significantly lower for scan and calibrated conditions than for uncalibrated condition
- for rifle θ_z error ($p = 0.0001$), θ_y error ($p = 0.0001$) and θ_x error ($p = 0.0001$) were significantly lower for scan and calibrated conditions than for uncalibrated condition

The results are illustrated in Fig. 8 and confirm the third hypothesis.

i. Fourth Hypothesis

Comparing errors from from combined images obtained with three stationary cameras to model overlay errors from combined images obtained from three locations of moving cameras, we found

- for motorbike r_{xyz} error ($p = 0.0029$), θ_z error ($p = 0.0333$), θ_y error ($p = 0.0144$) and θ_x error ($p = 0.003$) were significantly lower for stationary cameras than for moving cameras
- for rifle r_{xyz} error (p 0.005), θ_y error ($p = 0.0252$) and θ_x error ($p = = 0.0089$) were significantly lower for stationary cameras than for moving cameras but θ_z error ($p = 0.093$) was not significantly different

The results are illustrated in Figs. 9 and 10 and confirm the fourth hypothesis.

Discussion

The results of this study show the accuracy of placing a 3D model or measuring an object in a scene varies depending on the information available, but generally is in the order of centimetres, varying significantly based on the available supporting information and calibration. Studies involving measurement of the location of objects in an incident video which are no longer physically present at the site vary in their techniques and methodologies. Various methods of lens correction, number of cameras used, and object sizes and distances make it difficult to directly compare the results of these studies. However, our results fall within the ranges reported in previous studies regarding error in object placement through 2D image sources for forensic applications.

Studies employing similar photogrammetry techniques vary based on several factors, including camera quality, level of control, use of coded targets, viewing distance, etc. [16,30]. For example, a study by Gyemi et al., in 2021, demonstrated a position uncertainty error of 1.5 ± 0.3 cm when determining head impact velocities in American youth football games through multi-camera spatial intersection [30]. Notably, this error was associated with only a single point (the center of the player's head) and is therefore cannot be directly compared to the present study in which several measured points were used to position a 3D model, with the error calculated for model position rather than individual point accuracy. A more comparable study, conducted by Terpstra et al. [16] investigated the error in positioning 3D vehicle models within a 3D scene based on their locations seen in 2D images, employing similar techniques to those of the present study. Their average orientation error was 0.5 ± 0.4 deg and 10.4 ± 13.5 cm for positioning the 3D vehicle model, based on its location seen in 2D images [16]. In comparison, the results obtained in the present study, particularly with respect to the methodology using the 3D scan of the site as a reference, were equally accurate for object positioning and orientation, with errors of 6.52 ± 4.51 cm and approximately 0.5 deg, for the motorcycle using a single camera view.

The most important finding of this study was the accuracy in positioning and orienting the model achieved with ray pinning when incorporating a 3D scan of the incident scene. With single cameras, the mean error was less than 7 cm at a distance of approximately 7 m, i.e. approximately 1 % of the distance from the camera to the object. Furthermore, the mean orientation errors were well below 1 deg. Thus, forensic investigators can be confident that, when utilizing a site scan,

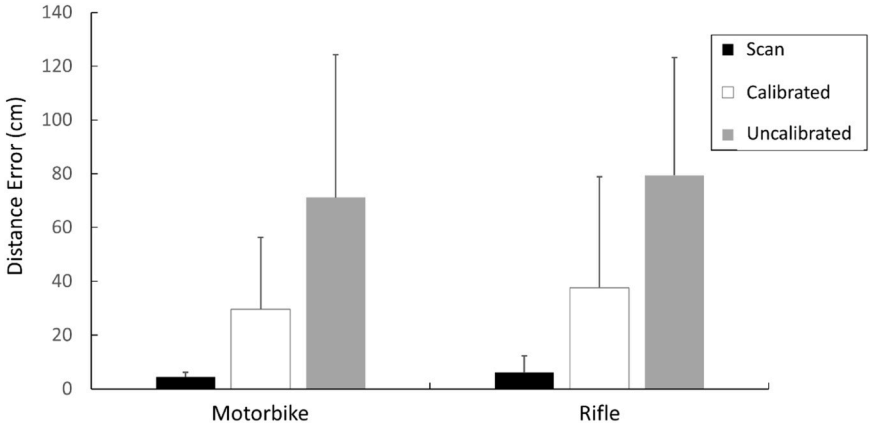

Fig. 7. Mean and standard deviation of model overlay distance errors compared for the three ray pinning methodologies applied to the 3-camera view.

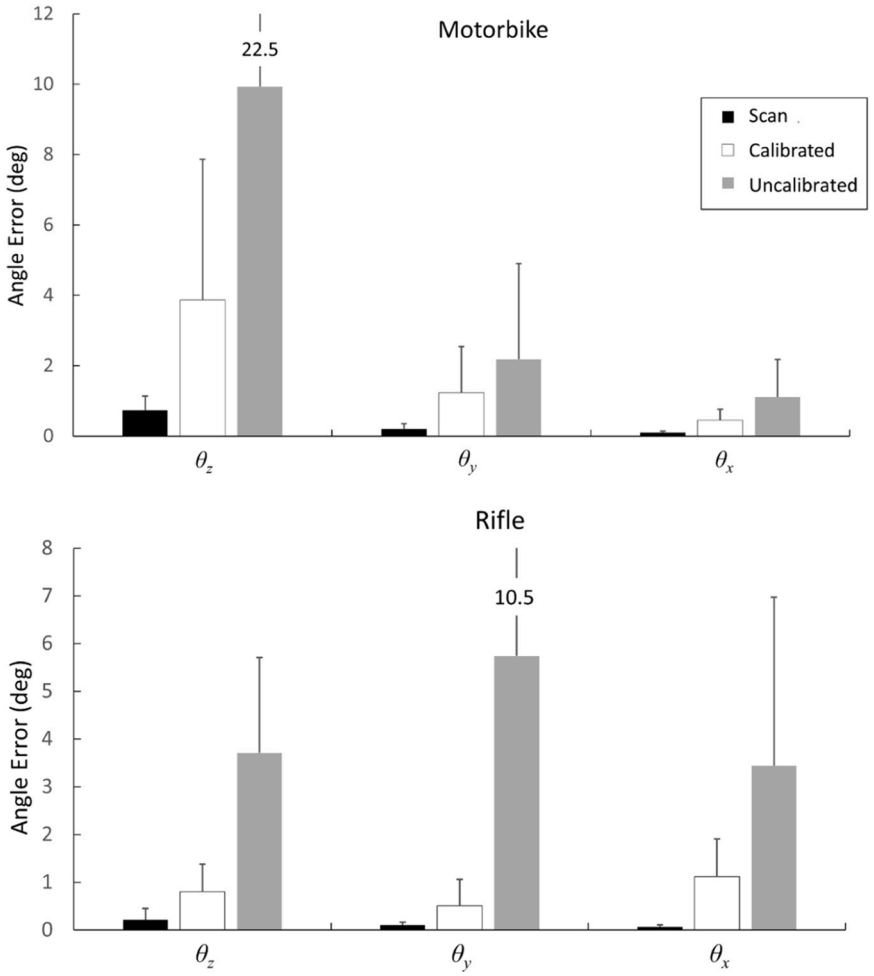

Fig. 8. Mean and standard deviation of model overlay orientation errors around each camera axis compared for the three ray pinning methodologies applied to the 3-camera view. Numbers on error bars indicate actual value at error cap, i.e. the largest error bars were truncated to facilitate comparison of mean values.

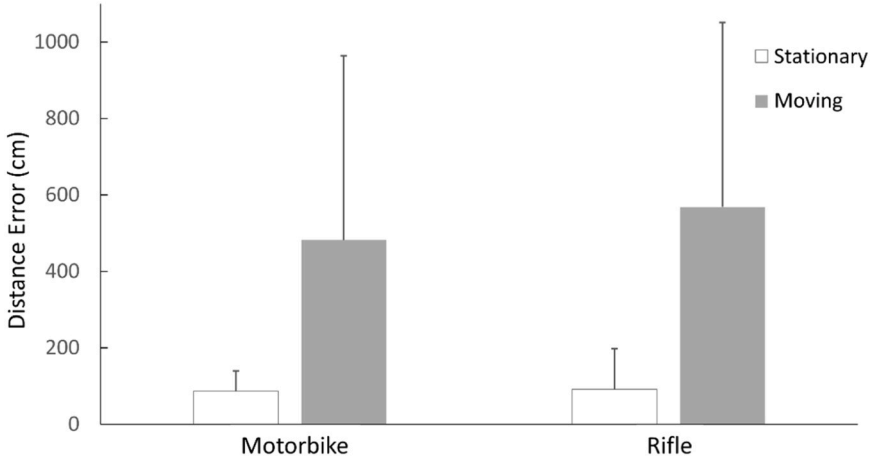

Fig. 9. Mean and standard deviation of model overlay distance errors compared for ray pinning with images form stationary and moving cameras.

photogrammetry provides accurate information which can be further used to draw conclusions about the incident.

The study also examined the relative errors in different camera planes. As predicted, for single camera views, the distance error was greater along the optical axis than in the focal plane of the camera. Although it was approximately twice as large along the optical axis, the size of the error relative to the distance of the object from the camera was still less than 1 %. While having multiple viewing angles allows for triangulation of specific 3D points to use as references for positioning the model [7–9], this is not the case with only one viewing angle. The single view results in lines which are projected from the camera through the specified 2D image [39]. For positioning in the focal plane, these lines provide sufficient constraint. However, for positioning along the optical axis, the control points on the ray-pinned model and the control lines

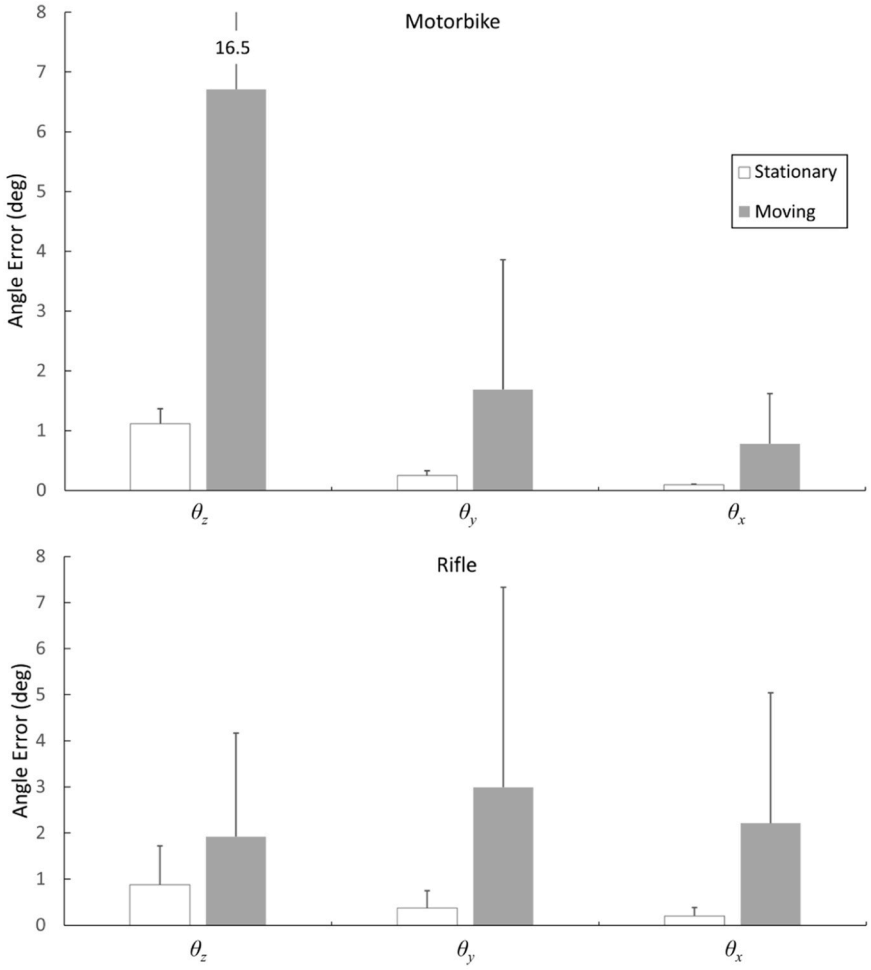

Fig. 10. Mean and standard deviation of model overlay orientation errors compared for ray pinning with images form stationary and moving cameras.

projected from the camera will align at any distance from the camera itself, only to be constrained by the known scale of the object. Therefore, small errors in the ray-pinned model's size, the defined scale of the incident scene, or the position of the control points placed on the image and model will result in large errors along the optical axis. This is an important consideration for forensics, as it implies that camera placement and viewing angle of the incident are important, and that measurements should be made within the focal plane of the viewing camera whenever possible.

With the multiple camera views, the ray-pinned model and the associated control points can be triangulated without the use of a 3D scan, providing 3D points instead of projected lines as described above [7–9]. This, in theory, increases both the focal plane and optical axis accuracy of the ray pinning operation compared with single views. As such, it was hypothesized that ray pinning using three simultaneous stationary cameras would be more accurate when compared to the single camera placements. However, the statistical analysis found no significant difference in distance error. While unexpected, this may be due to mismatch between the object and site feature points defined in each of the 3 camera images creating a discrepancy in the triangulated points used for spatial intersection and solving camera location. In addition, the three cameras were not identical creating substantial variability in the accuracy of the single camera views, which contributed to the lack of statistical significance. Using the same camera to obtain the different views would reduce the variability in accuracy. Back projecting a 2D view from the 3D scan onto the camera images could aid in selecting and positioning matching control points for more accurate triangulation.

While 3D scans and images calibrated for distortions are ideal when performing a forensic investigation, these may not always be available. Therefore, it is important to also quantify the error associated with the use of unknown, uncalibrated images. The extent of the effect of lens distortion is dependent on several factors, including the severity of the distortion and the placement of the object of interest or intended measurement within the frame [10]. When using uncalibrated images, these distortions remain and affect final measurements. We confirmed the hypothesis that the use of 3D scans or calibrated cameras for ray pinning would result in lower model placement errors when compared to the use of uncalibrated images. The mean errors for the uncalibrated images were much larger than for those using calibrated images or a scan, with the employment of a scan producing the greatest accuracy, as seen in Figs. 7 and 8. The large errors for the uncalibrated images, in the range of 14.72–138.78 cm, indicate a consistent failure to solve both the correct camera and object locations, likely due to unresolved high levels of distortion in the images. These findings should guide forensic specialists in selecting their method of inquiry when performing investigations, highlighting the benefit of a 3D incident site scan.

In many forensic investigations, images from stationary cameras may not be available, whereas there may be body worn camera or bystander mobile phone footage [3]. Consequently, we tested the accuracy of ray pinning by using images taken with a moving camera at three different positions. We hypothesized that using images from three stationary cameras would result in lower errors compared to using a moving camera at three different points in time, i.e. three different locations. There are several reasons for this hypothesis. Firstly, body worn cameras such as the AXON line may have lower resolution compared to

stationary cameras, such as security cameras, which are often referenced by forensic investigators. Additional reasons for this hypothesis include the effect of motion blur in the moving camera frames and the relatively small changes in viewing angle from frame to frame as compared to the stationary cameras, though viewing angles for moving cameras will change on a case by case basis with longer times between analyzed frames and distance to the objects of interest or increased velocity. The statistical analysis confirmed our hypothesis as measurements made with the stationary 3-camera solution was significantly more accurate than with the moving cameras for both distance and orientation errors.

Conclusions

The present study explored the accuracy of positioning and orienting an object in a 3D rendition of an incident scene, based on 2D images in which the object appears in the incident scene but is no longer present at the time of the forensic investigation. Several conditions affecting the accuracy of the ray pinning technique for object placement were analyzed, including the inclusion of a 3D scan, number of available camera views, the method of lens correction, and whether the cameras were stationary or in motion. We found that the use of 3D scans to aid in ray pinning resulted in lower distance and orientation errors compared to conditions lacking a scan, whether or not the camera has been calibrated for lens distortion. Using uncalibrated camera images proved least accurate by a significant margin. With a supporting 3D scan, there did not appear to be a significant difference between the single camera and stationary 3-camera for distance error, although this may have been partly due to the variability of using three different cameras. However, the single camera solution produced lower orientation errors. Furthermore, as hypothesized, the stationary 3-camera solution was more accurate than the moving camera solution.

As accurate analysis of incident sites is paramount to forensic investigations, the present study provides useful quantitative information regarding the accuracy of available methodologies to aid forensic investigators in making informed decision regarding their investigative approach. However, because the present study used models of the objects of interest which were generated from a 3D scan of the physical objects in the same location and orientation as photographed, it should be pointed out that larger errors can be expected when ray pinning is performed with less accurate 3D models of objects of investigative interest. Moreover, if 3D scans of an incident site do not occur immediately following the incident, features of the site may be altered. Thus, it is essential to only use features in the scan which correspond to features seen in images taken at the time of the incident. Overall, when performing photogrammetry to analyze an incident, 3D scans of the site should be generated immediately, to limit changes from the initial incident, whenever possible. If this cannot be done, performing a calibration of the cameras which recorded the videos or images of interest is a viable alternative. Furthermore, photogrammetry for forensic invesitgations may benefit from implementing technologies such as AI to more accurately locate corresponding features in 2D images and 3D models or LiDAR for incident scenes which cover very large areas.

CRediT authorship contribution statement

Desmoulin Geoffrey Thor: Writing – review & editing, Project administration, Funding acquisition, Conceptualization. **Kevin Gilmore:** Writing – original draft, Data curation. **Nolette Marc-Andre:** Visualization. **Szymon Claridad:** Visualization, Data curation. **Milner Theordore Edgar:** Writing – review & editing, Supervision, Methodology.

Declaration of Competing Interest

The authors have no conflict of interest as a result of being involved in this study and the entire study was funded internally by GTD Scientific Inc.

Appendix A. Known-Pattern Calibration RMS Residual Graphs

Figure A.1. Canon EOS 7D Calibration RMS Residuals Graph

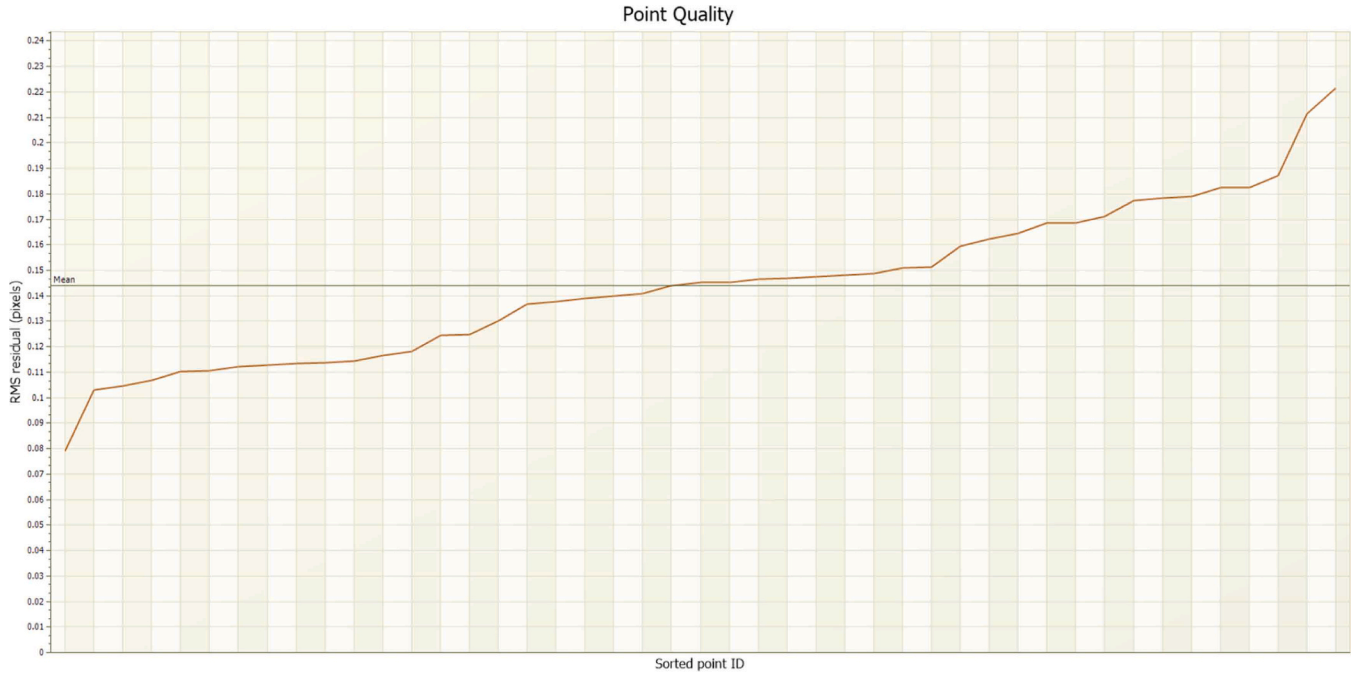

Figure A.2. GoPro Hero 8 Calibration RMS Residuals Graph

Figure A.3. GoPro Hero 11 Calibration RMS Residuals Graph

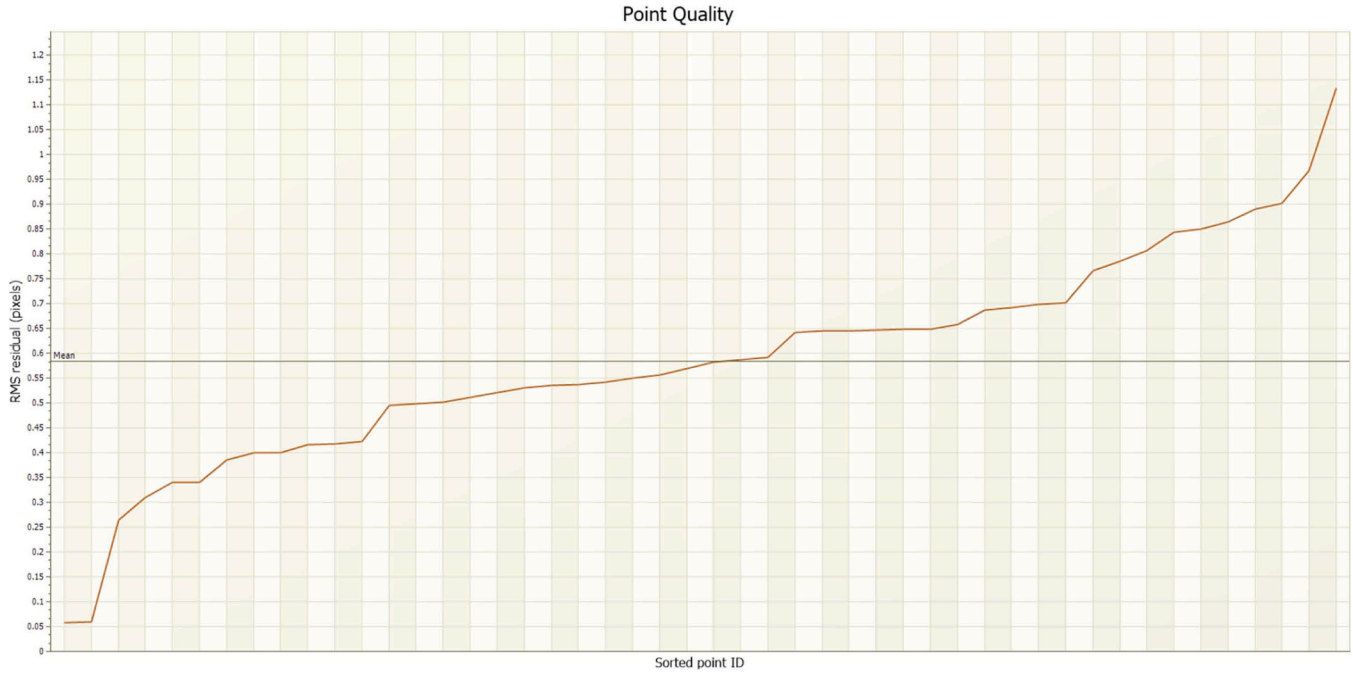

Figure A.4. AXON Body 2 Calibration RMS Residuals Graph

Figure A.5. Samsung Galaxy S22 Calibration RMS Residuals Graph

References

[1] M. Davoudkhani, C. Mulsow, H.-G. Maas, Single camera 6-DOF object tracking using spatial resection based techniques, Int. Arch. Photogramm. Remote Sens. Spat. Inf. Sci. XLVIII-G-2025 (2025) 351–358.
[2] T. Luhmann, Precision potential of photogrammetric 6DOF pose estimation with a single camera, ISPRS J. Photogramm. Remote Sens 64 (2009) 275–284.
[3] G.T. Desmoulin, M. Kalkat, T.E. Milner, Forensic application of inverse and reverse projection photogrammetry to determine subject location and orientation when both camera and subject move relative to the scene, For. Sci. Int. 331 (2022) 111145.
[4] P. Grussenmeyer, O.Al Khalil, Solutions for exterior orientation in photogrammetry: a review, Photogramm. Rec. 17 (2002) 615–634.
[5] S. Mikolka-Flöry, C. Ressl, L. Schimpl, N. Pfeifer, Automatic orientation of historical terrestrial images in mountainous terrain using the visible horizon, ISPRS Open J. Photogramm. Remote Sens 6 (2022).
[6] R. Rofallski, T. Luhmann, An efficient solution to ray tracing problems in multimedia photogrammetry for flat refractive interfaces, PFG J. Photogramm. Remote Sens. Geoinf. Sci. 90 (2022) 37–54.
[7] T. Luhmann, W. Tecklenburg, 3-D object reconstruction from multiple-station panorama imagery, ISPRS, Arch 34 (2004) 5.

[8] T. Luhmann, Eccentricity in images of circular and spherical targets and its impact on spatial intersection, Photogramm. Rec. 29 (2014) 417–433.
[9] T. Luhmann, Close range photogrammetry for industrial applications, ISPRS J. Photogramm. Remote Sens 65 (2010) 558–569.
[10] B. Pan, L. Yu, D. Wu, L. Tang, Systematic errors in two-dimensional digital image correlation due to lens distortion, Opt. Lasers Eng. 51 (2013) 140–147.
[11] E. Liscio, H. Guryn, Q. Le, A. Olver, A comparison of reverse projection and Photomodeler for suspect height analysis, For. Sci. Int. 320 (2021) 110690.
[12] W.T.C. Neale, S. Fenton, S. McFadden, N.A. Rose, A video tracking photogrammetry technique to survey roadways for accident reconstruction, SAE Tech. Pap. (2004) 2004–01-1221.
[13] T. Terpstra, T. Voitel, A. Hashemian, A survey of multi-view photogrammetry software for documenting vehicle crush, SAE Tech. Pap. (2016) 2016–01-1475.
[14] R. Rucoba, A. Duran, L. Carr, D. Erdeljac, A three-dimensional crush measurement methodology using two-dimensional photographs, SAE Tech. Pap. (2008) 2008–01-0163.
[15] C.C. Chou, R.W. McCoy, J.J. Le, S. Fenton, W. Neale, N. Rose, Image analysis of rollover crash tests using photogrammetry, SAE Tech. Pap. (2006) 2006–01-0723.
[16] T. Terpstra, A. Hashemian, R. Gillihan, E. King, S. Miller, W. Neale, Accuracies in single image camera matching photogrammetry, SAE Tech. Pap. (2021) 2021–01-0888.
[17] B. Epstein, B.G. Westlake, Determination of vehicle speed from recorded video using reverse projection photogrammetry and file metadata, J. For. Sci. 64 (2019) 1523–1529.
[18] S. Fenton, W. Neale, N. Rose, C. Hughes, Determining crash data using camera matching photogrammetric technique, SAE Tech. Pap. (2001), 2001-01-3313.
[19] W.T. Neale, J. Marr, D. Hessel, Video projection mapping photogrammetry through video tracking, SAE Tech. Pap. (2013), 2013-01-0788.
[20] B. Hoogeboom, I. Alberink, Measurement uncertainty when estimating the velocity of an allegedly speeding vehicle from images, J. For. Sci. 55 (2010) 1347–1351.
[21] P.K. Larsen, E.B. Simonsen, N. Lynnerup, Use of photogrammetry and biomechanical gait analysis to identify individuals, EUSIPCO2010 (2010) 1660–1664.
[22] A.F. Macedo Ribeiro, A. Bergmann, T. Lemos, A.G. Pacheco, M. Mello Russo, L. A. Santos de Oliveira, E. de Carvalho Rodrigues, Reference values for human posture measurements based on computerized photogrammetry: a systematic review, J. Manip. Physiol. Ther. 40 (2017) 156–168.
[23] T.S. Furlanetto, J.A. Sedrez, C.T. Candotti, J.F. Loss, Photogrammetry as a tool for the postural evaluation of the spine: a systematic review, World J. Orthop. 7 (2016) 136–148.
[24] I.C.N. Sacco, S. Alibert, B.W.C. Queiroz, D. D. Pripas, I. I. Kieling, A.A. Kimura, A. E. Sellmer, R.A. Malvestio, M.T. M.T. Sera, Reliability of photogrammetry in relation to goniometry for postural lower limb assessment, Rev. Bras. Fisiote 11 (2007) 411–417.
[25] W.L. Ripka, L. Ulbricht, P.M. Gewehr, Application of a photogrammetric kinematic model for prediction of lung volumes in adolescents: a pilot study, BioMed. Eng. OnLine 13 (2014) 21.
[26] M. Galetto, L. Gastaldi, G. Lisco, L. Mastrogiacomo, S. Pastorelli, Accuracy evaluation of a new stereophotogrammetry-based functional method for joint kinematic analysis in biomechanics, Proc. Inst. Mech. Eng. H. 228 (2014) 1183–1192.
[27] J. Davidson, A.M. dos Santos, K.M. Garcia, L.C. Yi, P.C. João, M.H. Miyoshi, A. L. Goulart, Photogrammetry: an accurate and reliable tool to detect thoracic musculoskeletal abnormalities in preterm infants, Physiotherapy 98 (2012) 243–249.
[28] L. Morales-Acosta, A. Ortiz-Prado, V.H. Jacobo-Armendáriz, R.A. González-Carbonell, Biomechanical analysis of weeding labor in Mexican farmers through the simultaneous use of photogrammetry and accelerometry, IFMBE 75 (2019) 850–857.
[29] D.J. Greencorn, D.I. Aponte, D.J. Pearsall, Photogrammetry: an accurate and cost-effective three-dimensional ice hockey helmet fit acquisition method, Proc. Inst. Mech. Eng. Part P 232 (2018) 334–341.
[30] D.L. Gyemi, D.M. Andrews, R. Jadischke, Three-dimensional video analysis of helmet-to-ground impacts in North American youth football, J. Biomech. 125 (2021) 110587.
[31] R. Walaszek, S. Sterkowicz, W. Chwała, K. Sterkowicz-Przybycień, K. Burdacka, M. Burdacki, Assessment of body posture with the Moire's photogrammetric method in boys practising judo versus their non-sports-practising peers, Sci. Sports 34 (2019) e187–e194.
[32] L.A. Magre Colorado, J.C. Martínez Santos, Kinematic parameter estimation using close range photogrammetry for sport applications, SPIE Proc. 9681 (2015) 96810M.
[33] A.M. Bailey, C.P. Sherwood, J.R. Funk, J.R. Crandall, N. Carter, D. Hessel, S. Beier, W. Neale, Characterization of concussive events in professional American football using videogrammetry, Ann. Biomed. Eng. 48 (2020) 2678–2690.
[34] D.L. Gyemi, R. Jadischke, D.M. Andrews, Validation of a multi-camera videogrammetry approach for quantifying helmet impact velocity in football, Sports Eng. 26 (2023) s12283-023-00423-7.
[35] A. Bailey, J. Funk, D. Lessley, C. Sherwood, J. Crandall, W. Neale, N. Rose, Validation of a videogrammetry technique for analysing American football helmet kinematics, Sports Biomech. 19 (2018) 678–700.
[36] D. Treccani, A. Adami, L. Fregonese, Assessing the effectiveness of lidar-based apps on Apple devices to survey indoor and outdoor medium sized areas, Int. Arch. Photogramm. Remote Sens. Spat. Inf. Sci. XLVIII-2/W8-2024 (2024) 431–438.
[37] D415, ⟨https://realsenseai.com/stereo-depth-cameras/stereo-depth-camera-d415/⟩ (accessed 2 Oct. 2025).
[38] M. Servi, A. Profili, R. Furferi, Y. Volpe, Comparative evaluation of Intel RealSense D415, D435I, D455, and microsoft azure kinect DK sensors for 3D vision applications, IEEE Access 12 (2024) 111311–111321.
[39] PhotoModeler, PhotoModeler Online user manual, ⟨https://www.photomodeler.com/downloads/OnlineHelp/index.html⟩ (accessed 2 Oct. 2025).
[40] B. Kraszewski, Calibration of digital SLR Nikon D3X for the use in digital photogrammetry projects, Inst. Geod. Cartogr. GeoInf. 1 (2011) 51–60.
[41] A. Basha, et al., Use of PhotoModeler as a measuring and management tool in construction projects, Glob. J. Eng. Technol. Adv. 10 (2022) 32–42.
[42] S. Karmakar, C.J. Turner, Non-invasive calibration of a Stewart platform by photogrammetry, Int. J. Adv. Manuf. Technol. 132 (2024) 2601–2616.
[43] P. Chen, J. Liu, Q. Zhong, High-speed videogrammetric technique for displacement measurement of floating offshore wind turbine model, Proc. Int. Conf. Digit. Image Process 14 (2022) 28.